Magnetic Equivalent Circuit Modeling of Induction Machines under Stator and Rotor Fault Conditions

Gennadi Y. Sizov, *IEEE Student Member*, Chia-Chou Yeh, *IEEE Member*,
Nabeel A. O. Demerdash, *IEEE Life-Fellow*

***Abstract* – In this paper, stator and rotor failures in squirrel-cage induction machines are modeled using the magnetic equivalent circuit (MEC) approach. Failures associated with stator winding and rotor cage are considered. More specifically, stator inter-turn short circuit and broken rotor bar failures are modeled. When compared to conventional modeling techniques, the MEC modeling approach offers two main advantages: 1) relatively high speed of execution, and 2) high accuracy. The developed MEC model is validated here with respect to the experimental tests and time-stepping finite-element simulations for healthy and various faulty conditions.**

***Index Terms* – Induction machines, magnetic equivalent circuit (MEC), fault modeling, rotor faults, stator winding faults.**

I. Introduction

NUMEROUS induction machine models have been developed over the years. These models range from the simplest T-equivalent circuit models, described in [1], to more sophisticated ones such as: multiple coupled circuit models [2], magnetic equivalent circuit models, also known as the permeance network models, [3]-[7], and the finite-element (FE) models [8]. Application of the specific model to a specific task depends on the level of desired accuracy, computational time, as well as the complexity of the physical phenomenon that needs to be captured in the solution. In fault simulation studies, the complexity of the model depends on the type of fault that needs to be studied. For simulation of stator winding and rotor cage failures, the magnetic equivalent circuit (MEC) modeling approach offers a good balance between the execution time and solution accuracy. Magnetic equivalent circuit models provide reasonably accurate results and relatively fast computation time, when compared to the time-stepping finite-element (TSFE) models. Finite-element models, in general, provide a higher degree of space discretization, and hence a more accurate solution, when compared to the MEC approach. However, the computational times required by such TSFE models are significantly longer due to their complexity.

The magnetic equivalent circuit modeling approach has been successfully used to model a variety of electric machines under various healthy and faulty conditions [3]-[6]. More specifically, the MEC modeling approach has been used to model induction machines under a variety of steady-state and transient conditions in [3] and [4]. A three-dimensional MEC model has been used in the study of inter-bar currents and the resulting axial fluxes in healthy and faulty induction machines in [5]. In [6] the MEC model has been shown to yield accurate results under a variety of operating conditions: no-load, rated-load, unbalanced excitation, and broken end-ring conditions.

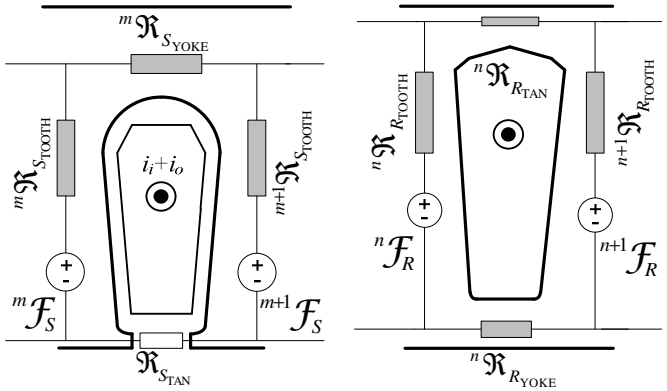

Fig. 1. Simplified MEC representation of: (a) double-layer stator winding. (b) rotor slot (without deep-bar effect).

In this paper, the development and validation of an MEC model that can simulate both stator inter-turn short circuit faults and broken (cracked) rotor bar faults are presented. The MEC model is verified by comparison of its results with TSFE simulations and experimental data for a case-study 5-hp squirrel-cage induction motor.

II. Induction Machine Modeling – Magnetic Equivalent Circuit (MEC) Approach

In this section, development of a magnetic equivalent circuit (MEC) model for fault simulation studies is discussed. In this work, the model has been developed using the formulation outlined in [3]. The MEC modeling approach allows one to incorporate space-harmonics due to discrete winding distributions, stator and rotor slotting, as well as saliency effects caused by saturation of the magnetic materials in the stator and rotor cores [3] and [4]. Moreover, deep-bar effects can be included in the solution to provide a more realistic transient model of the machine [3].

A case-study 5-hp, 60-Hz, 6.8-A, 1165-r/min, 0.777-p.f., squirrel-cage induction machine, with 36 stator slots and 45 rotor slots/bars, has a double-layer stator winding with the layout phase designations shown in Table I. In Table I "Outer" refers to the part of the stator slot closest to the air-gap, whereas "Inner" refers to the part of the slot closest to the stator back-iron/yoke. Moreover, this machine has two slots per pole per phase, and a total of 36 coils, with 20 turns per coil, leading to 240 turns per phase.

A stator slot with a double-layer winding, such as any of the slots shown in Table I, can be represented by a simplified

This work is supported by the United States Department of Education under GAANN Grant No. P200A010104, and the National Science Foundation under Grant No. ECS-0322974.

Gennadi Y. Sizov and Nabeel A. O. Demerdash, are with the Department of Electrical and Computer Engineering, Marquette University, Milwaukee, WI 53233 USA (email: gennadi.sizov@mu.edu; nabeel.demerdash@mu.edu).
Chia-Chou Yeh is with the Powertrain Advanced Technology Center, General Motors Corporation, Torrance, CA 90505 USA (e-mail: chou.yeh@gm.com).

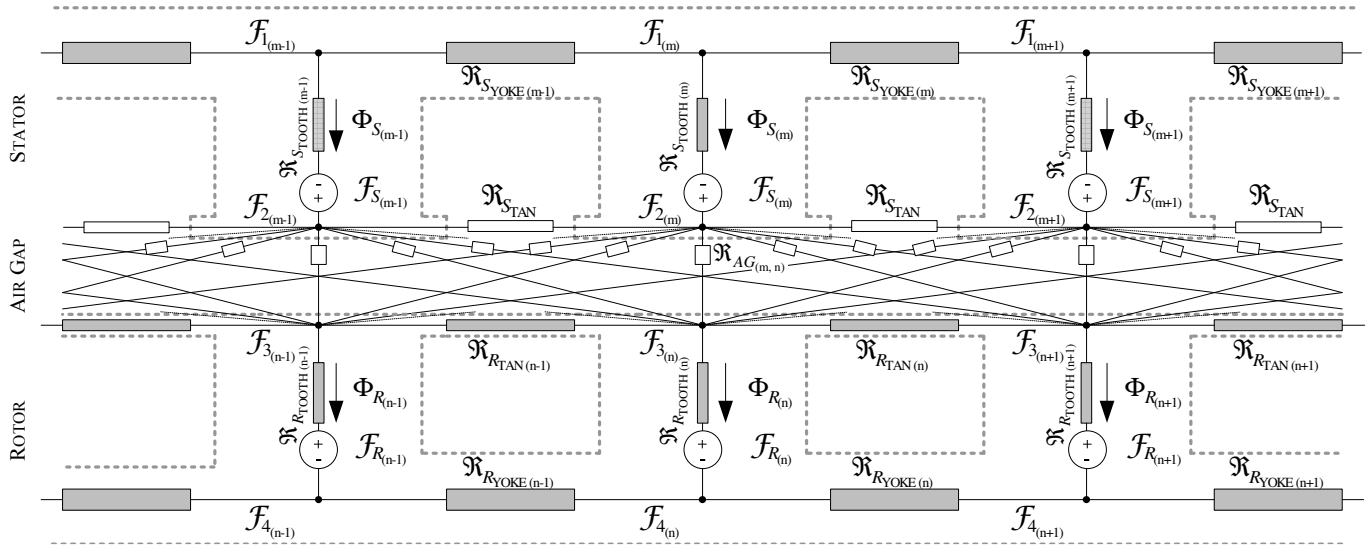

Fig. 2. MEC representation of the 5-hp induction machine (with closed rotor slot).

magnetic equivalent circuit [4] shown in Fig. 1 (a). Assuming steady-state operation with no deep-bar effects, the rotor slot can be modeled as shown in Fig. 1 (b).

It should be highlighted that the MEC modeling approach can be utilized for various transient simulations if the rotor slot is divided into a sufficient number of sections in order to accommodate deep-bar effects [3]. Another approach of including the deep-bar effect is by updating the reactance of the rotor bar (depending on the rotor speed) at every time-step of the simulation.

In order to include the saturation effects, the reluctance values representing the regions of the machine where the magnetic material is present can be varied, depending on the values of the flux densities in the individual stator and rotor teeth. It should be noted that in Figs. 1 (a) and (b), the indices, *m* and *n*, are used to distinguish between the various individual stator and rotor teeth reluctances, which may vary if saturation needs to be considered.

A complete MEC model of the induction machine is depicted in Fig. 2. From this figure it should be noted that the MEC model is assembled such that every tooth on the stator is coupled to every tooth on the rotor, and vice versa. Air-gap reluctances depend on the relative position of the corresponding stator and rotor teeth. More specifically, an air-gap reluctance is a function of the area of overlap of stator and rotor teeth. From Fig. 2 one can proceed with the development of the system of algebraic equations governing the nodal magnetic scalar potentials (msps/mmfs). The nodal-potential method can be used to generate the required equations. To avoid possible numerical difficulties in a computer simulation associated with possibilities of dealing with infinite air-gap reluctances one should inverse the reluctance values to obtain the corresponding permeance values. The nodal mmfs used to generate the equations are: $\mathcal{F}_{1_{(m)}}$, $\mathcal{F}_{2_{(m)}}$, $\mathcal{F}_{3_{(n)}}$, $\mathcal{F}_{4_{(n)}}$, where the index, *m*, identifies a stator tooth and the index, *n*, is used to identify a rotor tooth. Hence, in the case-study motor with a number of stator slots, $N_S=36$ slots, rotor slots, $N_R=45$ slots, the index, *m*, varies from 1 to 36, and the index, *n*, varies from 1 to 45. Considering Fig. 2 with the reluctances substituted for with the corresponding permeances, one can develop four sets of nodal equations as follows:

$$\begin{bmatrix} \underline{\mathbf{A}}_{11} & \underline{0} & \underline{0} & \underline{0} \\ \underline{0} & \underline{\mathbf{A}}_{22} & \underline{\mathbf{A}}_{23} & \underline{0} \\ \underline{0} & \underline{\mathbf{A}}_{32} & \underline{\mathbf{A}}_{33} & \underline{0} \\ \underline{0} & \underline{0} & \underline{0} & \underline{\mathbf{A}}_{44} \end{bmatrix} \begin{bmatrix} \underline{\boldsymbol{\mathcal{F}}}_1 \\ \underline{\boldsymbol{\mathcal{F}}}_2 \\ \underline{\boldsymbol{\mathcal{F}}}_3 \\ \underline{\boldsymbol{\mathcal{F}}}_4 \end{bmatrix} = \begin{bmatrix} -\underline{\boldsymbol{\Phi}}_S \\ \underline{\boldsymbol{\Phi}}_S \\ -\underline{\boldsymbol{\Phi}}_R \\ \underline{\boldsymbol{\Phi}}_R^{'} \end{bmatrix} \quad (1)$$

where, the vector/array of rotor teeth fluxes, $\underline{\boldsymbol{\Phi}}_R^{'}$, is expressed as follows:

$$\underline{\boldsymbol{\Phi}}_R^{'} = [\Phi_{\mathrm{R}_{(1)}} \quad \Phi_{\mathrm{R}_{(2)}} \quad \Phi_{\mathrm{R}_{(3)}} \quad \cdots \quad \Phi_{\mathrm{R}_{(N_R-1)}}]^{\mathrm{T}} \quad (2)$$

In order to provide a relationship between the nodal mmf vectors, $\underline{\boldsymbol{\mathcal{F}}}_1$, $\underline{\boldsymbol{\mathcal{F}}}_2$, $\underline{\boldsymbol{\mathcal{F}}}_3$, $\underline{\boldsymbol{\mathcal{F}}}_4$, and the corresponding individual stator and rotor tooth mmf vectors, $\underline{\boldsymbol{\mathcal{F}}}_S$, $\underline{\boldsymbol{\mathcal{F}}}_R$, produced by the current carrying coil sides, two additional sets of equations have to be introduced. From the magnetic circuit of Fig. 2 these equations can be derived as follows:

$$\underline{\boldsymbol{\mathcal{F}}}_S = \underline{\boldsymbol{\mathcal{F}}}_2 - \underline{\boldsymbol{\mathcal{F}}}_1 + \underline{\boldsymbol{\mathfrak{R}}}_S \underline{\boldsymbol{\Phi}}_S \quad (3)$$

$$\underline{\boldsymbol{\mathcal{F}}}_R = \underline{\boldsymbol{\mathcal{F}}}_3 - \underline{\boldsymbol{\mathcal{F}}}_4^{'} - \underline{\boldsymbol{\mathfrak{R}}}_R \underline{\boldsymbol{\Phi}}_R \quad (4)$$

where, $\underline{\boldsymbol{\mathcal{F}}}_4^{'} = [\mathcal{F}_{4_{(1)}} \quad \mathcal{F}_{4_{(2)}} \quad \mathcal{F}_{4_{(3)}} \quad \cdots \quad \mathcal{F}_{4_{(N_R-1)}} \quad 0]^{\mathrm{T}}$. Also, $\underline{\boldsymbol{\mathfrak{R}}}_S$, and, $\underline{\boldsymbol{\mathfrak{R}}}_R$, are the diagonal matrices of the stator and rotor teeth reluctances. In order to derive a relationship between the stator phase flux linkages, λ_a, λ_b, λ_c, and the individual stator tooth

TABLE I. STATOR WINDING LAYOUT OF THE 5-HP SQUIRREL-CAGE INDUCTION MACHINE.

Inner	A+	C-	C-	B+	B+	A-	A-	C+	C+	B-	B-	A+	A+	C-	C-	B+	B+	A-	A-	C+	C+	B-	B-	A+	A+	C-	C-	B+	B+	A-	A-	C+	C+	B-	B-	A+
Outer	A+	A+	C-	C-	B+	B+	A-	A-	C+	C+	B-	B-	A+	A+	C-	C-	B+	B+	A-	A-	C+	C+	B-	B-	A+	A+	C-	C-	B+	B+	A-	A-	C+	C+	B-	B-	
Slot	*1*	*2*	*3*	*4*	*5*	*6*	*7*	*8*	*9*	*10*	*11*	*12*	*13*	*14*	*15*	*16*	*17*	*18*	*19*	*20*	*21*	*22*	*23*	*24*	*25*	*26*	*27*	*28*	*29*	*30*	*31*	*32*	*33*	*34*	*35*	*36*	

fluxes, $\underline{\mathbf{\Phi}}_S$, and the stator line currents, i_a, i_b, i_c, and the individual tooth mmfs, $\underline{\mathcal{F}}_S$, one has to consider the stator winding layout provided in Table I. An analytical approach to developing the relationships between the stator phase flux linkages and individual stator teeth fluxes, and the stator phase currents and individual stator teeth mmfs, based on parameters such as: the type of winding, the number of slots, the number coils per pole per phase, the winding connection, etc., has been developed in [3]. For this case-study 5-hp squirrel-cage induction machine, with a double-layer winding given in Table I, these relationships are provided in (5) and (6), below:

$$\underline{\boldsymbol{\lambda}}_{abc} = N\underline{\mathbf{w}}'\underline{\mathbf{\Phi}}_S \tag{5}$$

$$\underline{\mathcal{F}}_S = \underline{\mathbf{w}}''\underline{\mathbf{i}}_{abc} \tag{6}$$

where, N, is the number of turns per coil, and $\underline{\mathbf{w}}'$ as well as $\underline{\mathbf{w}}''$, have been defined as flux and mmf connection matrices in [3]. For the squirrel-cage rotor the procedure is greatly simplified. In a squirrel-cage rotor, the teeth fluxes, $\underline{\mathbf{\Phi}}_R$, are equal to the rotor loop flux linkages, $\underline{\boldsymbol{\lambda}}_R$ and the rotor teeth mmfs, $\underline{\mathcal{F}}_R$, are equal to the rotor loop currents, $\underline{\mathbf{i}}_R$.

A complete system of equations that governs the magnetic equivalent model, with phase linkages, λ_a, λ_b, λ_c, and rotor teeth fluxes, $\underline{\mathbf{\Phi}}_R$, as inputs, and phase currents, i_a, i_b, and i_c, as outputs, is given in (7). In (7), $\underline{\mathbf{I}}_{k\times k}$, refers to an identity matrix of appropriate dimensions and, $\underline{\mathbf{I}}_{k\times k-1}$, refers to an identity matrix with the last column eliminated/truncated. The system of equations given in (7) can be simplified as has been done in [4]. The expression for electromagnetic torque can be derived, based on electromechanical energy conversion principles, from the MEC model directly and is given as follows:

$$T_{em} = \frac{1}{2}\sum_{\mathrm{m}=1}^{N_S}\sum_{\mathrm{n}=1}^{N_R}(\mathcal{F}_{2_{(\mathrm{m})}} - \mathcal{F}_{3_{(\mathrm{n})}})^2\frac{dP_{AG_{(\mathrm{m,n})}}}{d\theta_R} \tag{8}$$

where, θ_R, is the rotor position in mechanical radians and,

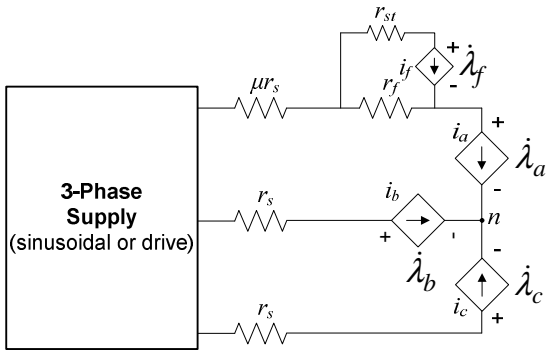

Fig. 3. Stator winding under inter-turn short circuit fault conditions.

$P_{AG_{(\mathrm{m,n})}}$, is the air-gap permeance between the m^{th} stator tooth and the n^{th} rotor tooth. The parameters of the MEC model for the case-study 5-hp induction machine are provided in the appendix. It should be noted that if saturation of the magnetic material does not need to be considered, the value of the relative permeability, $\mu_R = 11000$, in the linear region of the B-H curve, can be used for reluctance and permeance calculations.

A. *Stator Winding Faults* (*Inter-Turn Short Circuits*)

In order to simulate stator inter-turn short circuit faults two tasks have to be accomplished:

1) additional state variables have to be included to account for the shorted/faulty turns (fault flux linkage, λ_f, and faulty loop current, i_f),
2) the mmf and flux connection matrices, $\underline{\mathbf{w}}'$ and $\underline{\mathbf{w}}''$, have to be modified accordingly.

Assuming that the inter-turn short circuit failure occurs in phase-a of a wye-connected machine, the transient electric circuit model of the machine can be represented as shown in Fig. 3. In Fig. 3, r_s is the stator per phase resistance (provided in Table A-I of the appendix), r_f, is the fault resistance representing the stage of partial insulation failure before the occurrence of a complete solid-short between the turns,

$$\begin{bmatrix}
\underline{\mathbf{A}}_{11} & \underline{0} & \underline{0} & \underline{0} & \underline{0} & \underline{0} & \underline{\mathbf{I}}_{N_S\times N_S} & \underline{0} & \underline{0} \\
\underline{0} & \underline{\mathbf{A}}_{22} & \underline{\mathbf{A}}_{23} & \underline{0} & \underline{0} & \underline{0} & -\underline{\mathbf{I}}_{N_S\times N_S} & \underline{0} & \underline{0} \\
\underline{0} & \underline{\mathbf{A}}_{32} & \underline{\mathbf{A}}_{33} & \underline{0} & \underline{0} & \underline{0} & \underline{0} & \underline{0} & \underline{0} \\
\underline{0} & \underline{0} & \underline{0} & \underline{\mathbf{A}}_{44} & \underline{0} & \underline{0} & \underline{0} & \underline{0} & \underline{0} \\
-\underline{\mathbf{I}}_{N_S\times N_S} & \underline{\mathbf{I}}_{N_S\times N_S} & \underline{0} & \underline{0} & -\underline{\mathbf{I}}_{N_S\times N_S} & \underline{0} & \underline{\Re}_S & \underline{0} & \underline{0} \\
\underline{0} & \underline{0} & -\underline{\mathbf{I}}_{N_R\times N_R} & \underline{\mathbf{I}}_{N_R\times N_R-1} & \underline{0} & \underline{0} & \underline{0} & \underline{\mathbf{I}}_{N_R\times N_R} & \underline{0} \\
\underline{0} & \underline{0} & \underline{0} & \underline{0} & \underline{\mathbf{I}}_{N_S\times N_S} & -\underline{\mathbf{w}}'' & \underline{0} & \underline{0} & \underline{0} \\
\underline{0} & \underline{0} & \underline{0} & \underline{0} & \underline{0} & \underline{0} & \underline{\mathbf{w}}' & \underline{0} & \underline{0} \\
\underline{0} & \underline{0} & \underline{0} & \underline{0} & \underline{0} & \underline{0} & \underline{0} & \underline{\mathbf{I}}_{N_R\times N_R} & -\underline{\mathbf{I}}_{N_R\times N_R}
\end{bmatrix}
\begin{bmatrix}
\underline{\mathcal{F}}_1 \\ \underline{\mathcal{F}}_2 \\ \underline{\mathcal{F}}_3 \\ \underline{\mathcal{F}}'_4 \\ \underline{\mathcal{F}}_S \\ \underline{\mathbf{i}}_{abc} \\ \underline{\mathbf{\Phi}}_S \\ \underline{\mathcal{F}}_R \\ \underline{\mathbf{i}}_R
\end{bmatrix}
=
\begin{bmatrix}
\underline{0} \\ \underline{0} \\ -\underline{\mathbf{\Phi}}_R \\ \underline{\mathbf{\Phi}}'_R \\ \underline{0} \\ -\underline{\Re}_R\underline{\mathbf{\Phi}}_R \\ \underline{0} \\ \underline{\boldsymbol{\lambda}}_{abc}/N \\ \underline{0}
\end{bmatrix} \tag{7}$$

$$\underline{\mathbf{w}}' = (\underline{\mathbf{w}}'')^T =
\begin{bmatrix}
\frac{N-N_{st}}{N} & \frac{2N-N_{st}}{N} & \frac{2N-N_{st}}{N} & \frac{2N-N_{st}}{N} & \frac{2N-N_{st}}{N} & 1 & \cdots & -1 \\
-2 & -2 & -2 & -1 & 1 & 2 & \cdots & -2 \\
2 & -1 & -2 & -2 & -2 & -2 & \cdots & 2 \\
\frac{N_{st}}{N} & \frac{N_{st}}{N} & \frac{N_{st}}{N} & \frac{N_{st}}{N} & \frac{N_{st}}{N} & 0 & \cdots & 0
\end{bmatrix}_{4\times N_S} \tag{9}$$

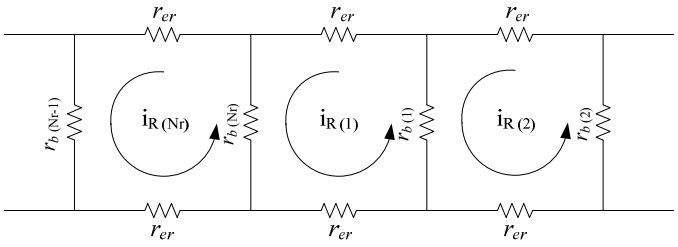

Fig. 4. Squirrel-cage rotor showing rotor loop currents.

$r_{st}=(N_{st}/N_{ph})r_s$, is the resistance of the shorted portion of the winding, where N_{st} is the number of shorted turns, and N_{ph} is the number of turns per phase, and the factor, $\mu=(N_{ph}-N_{st})/N_{ph}$, is the ratio of the remaining (healthy) number of turns to the total number of turns per phase. Furthermore, assuming that the inter-turn short circuit failure occurs in a portion of the first coil of phase-a (slots 1 and 6 of Table I), the connection matrices can be accordingly modified as given in (9).

B. Rotor Faults (*Broken/Cracked Bar*)

An electric connection of a squirrel-cage rotor is shown in Fig. 4. Depicted in Fig. 4 are bar resistances, r_b, and end ring connector resistances, r_{er}, of the squirrel-cage rotor (provided in Table A-I of the appendix). One simple way of simulating rotor broken bar faults in the MEC model is by increasing the resistance, $r_{b(Nr)}$, corresponding to the broken (or cracked) bar.

A functional block diagram of the complete MEC model coupled to the electrical and mechanical systems associated with the motor and its load is given in Fig. 5. It should be pointed out that the MEC block in Fig. 5 directly outputs the currents and developed torque from knowledge of the flux linkages and the rotor position. It should also be mentioned that the developed MEC model has been implemented in a MATLAB/Simulink (SimPowerSystems) environment. Accordingly, the developed MEC model is applicable to simulation of a motor supplied from direct-line sinusoidal excitation or from PWM-type drive, hence, enabling simulation of a complete motor-drive-controller system, if such a comprehensive simulation is needed.

TABLE II. STEADY-STATE PERFORMANCE UNDER HEALTHY CONDITIONS (MEC SIMULATIONS AND EXPERIMENTAL TESTS).

100% (30Nm)	**MEC**	**Experimental Test**
Current, [A_{rms}]	*6.10*	*6.15*
Speed, [r/min]	*1166*	*1165*
Power factor, [%]	*82.9*	*79.7*
75% (22.5Nm)	**MEC**	**Experimental Test**
Current, [A_{rms}]	*4.83*	*4.75*
Speed, [r/min]	*1175*	*1175*
Power factor, [%]	*76.8*	*74.2*
50% (15Nm)	**MEC**	**Experimental Test**
Current, [A_{rms}]	*3.91*	*3.95*
Speed, [r/min]	*1184*	*1182*
Power factor, [%]	*67.5*	*66.5*

IV. MODEL VALIDATION – SIMULATION AND EXPERIMENTAL RESULTS

The developed MEC model has been verified by comparing the results of the simulations with experimentally obtained data under sinusoidal supply excitation for healthy and various faulty conditions as given next.

A. Healthy Operation

Here, simulation and experimental results are presented for the machine operating at healthy, steady-state conditions. Depicted in Figs. 6a and 6b are the frequency spectra of the phase-a current, i_a, obtained from the MEC simulation and the experimental test. Also, provided in Table II are the tabulated data of the steady-state performance characteristics under healthy conditions at different levels of load.

B. Stator Winding Faults (*Inter-Turn Short Circuits*)

Here, the simulation and experimental results for the machine operating under the conditions of stator inter-turn short circuit failure are presented. Depicted in Figs. 7a, 7b, and 7c are the time-domain profiles of the phase-a current, i_a, shorted loop current, i_f, and the current passing through the fault resistance, i_{rf}, for the conditions of two shorted turns, $N_{st}=2$, and fault resistance, $r_f = 0.1\Omega$, obtained via the MEC simulation, the TSFE (developed in MAGSOFT-FLUX 2D) simulation and experimental test, respectively. It should be

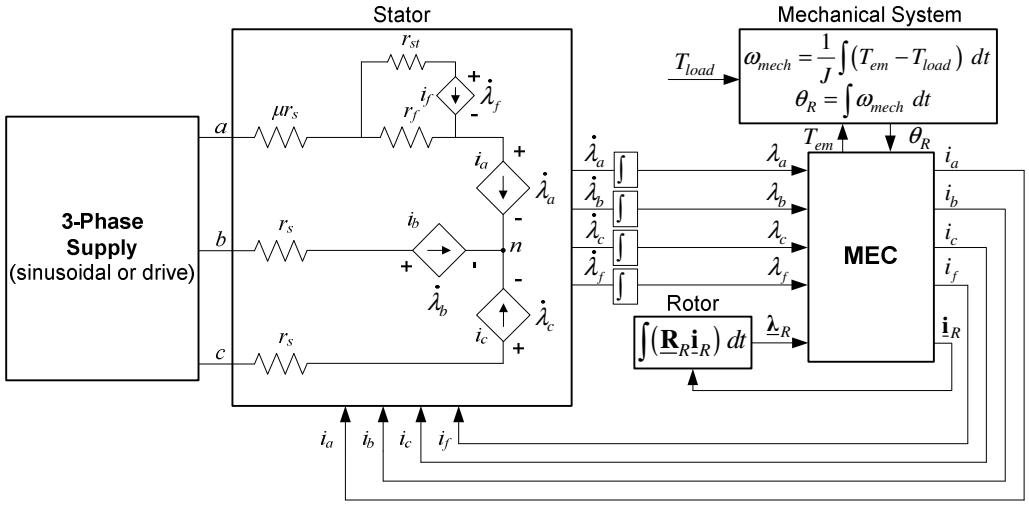

Fig. 5. Block diagram of a complete squirrel-cage induction machine MEC model.

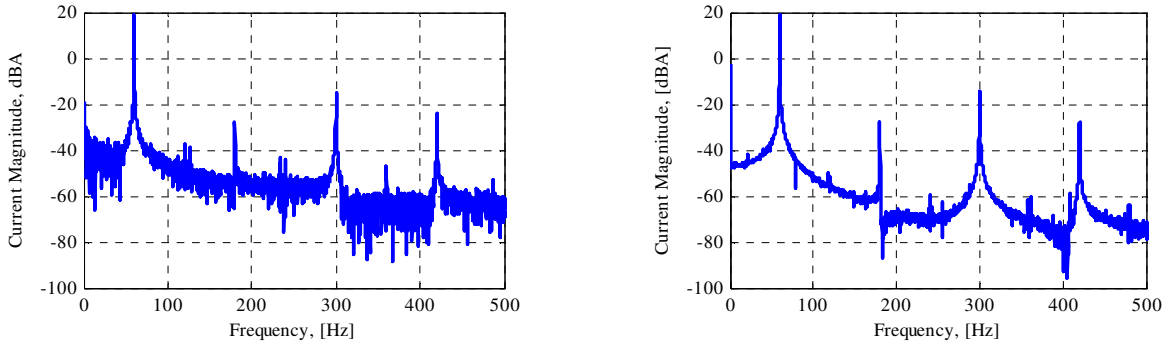

(a) **MEC Simulation** (supplied with measured voltages). (b) **Experimental Test**

Fig. 6. Frequency spectrum of phase-a current, i_a, under healthy, rated conditions (30Nm, 1165r/min): (a) MEC Simulation (supplied with measured voltages) and (b) Experimental Test.

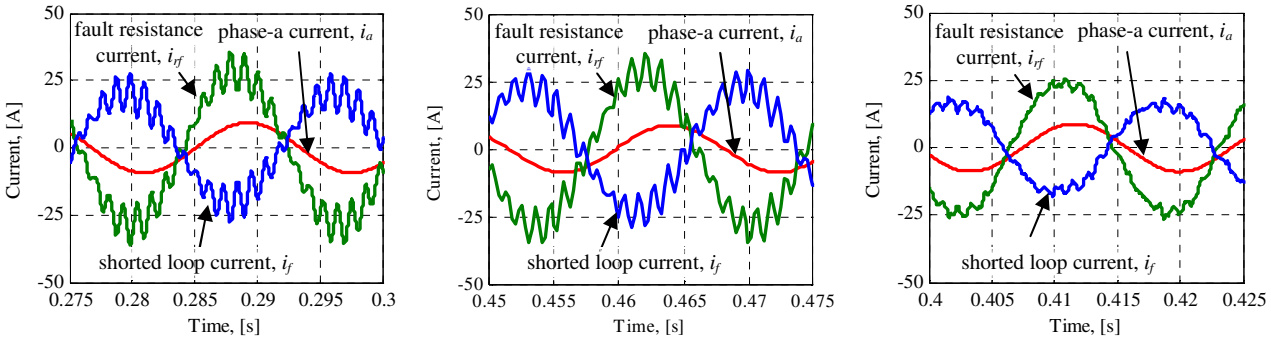

(a) **MEC Simulation** (b) **TSFE Simulation** (c) **Experimental Test** (r_f=*0.103*Ω)

Fig. 7. Time-domain profiles of phase-a current, i_a, shorted loop current, i_f, and fault resistance current, i_{rf}, under conditions of two turns shorted, N_{st}=*2*, through r_f=*0.1*Ω (30Nm, 1165r/min): (a) MEC Simulation, (b) TSFE Simulation and (c) Experimental Test.

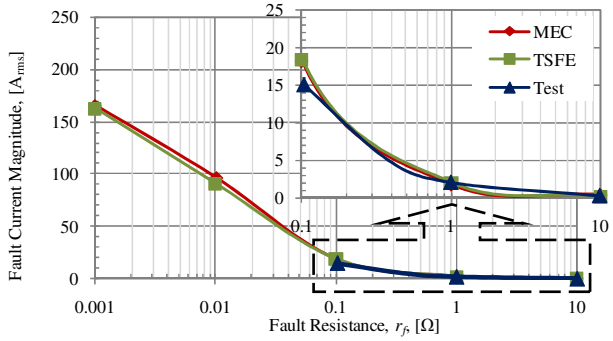

Fig. 8. Fault resistance current, i_{rf}, as a function of fault resistance, r_f, for two shorted turns, N_{st} = *2*.

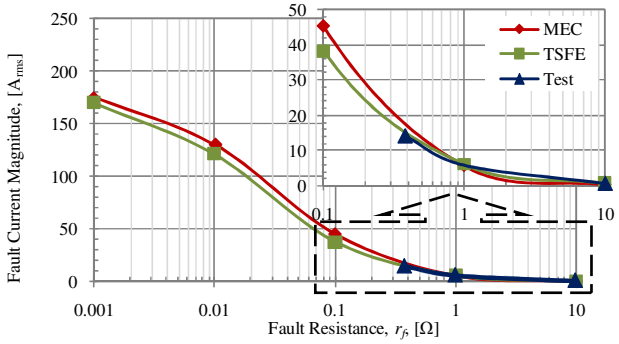

Fig. 9. Fault resistance current, i_{rf}, as a function of fault resistance, r_f, for two shorted turns, N_{st} = *6*.

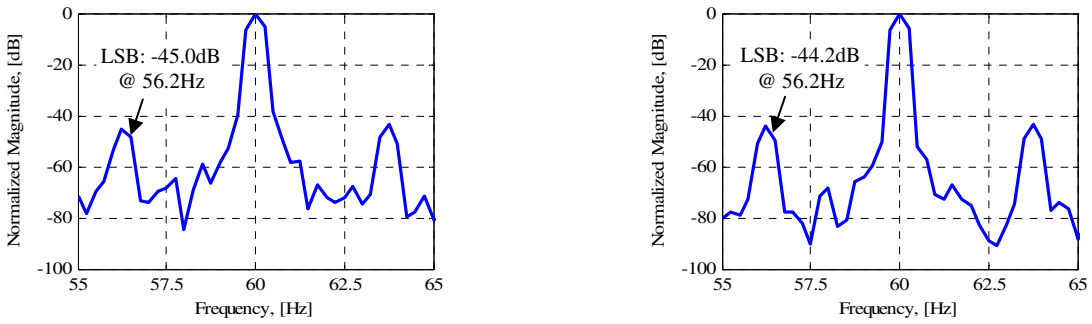

(a) **MEC Simulation** (supplied with measured voltages) (b) **Experimental Test**

Fig. 10. Frequency spectrum of phase-a current, i_a, under one broken bar condition (30Nm, 1165r/min): (a) MEC (b) Experiment

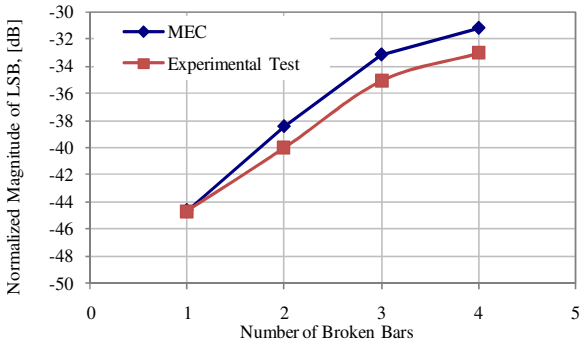

Fig. 11. Lower side band, LSB, component as a function of number of broken bars, rated load (30Nm, 1165r/min).

pointed out that the currents, i_a, i_f, and i_{rf}, in Figs. 7a, 7b, and 7c, are related by the following relationship, $i_{rf} = i_a - i_f$, see Fig. 5. Furthermore, the higher harmonic content in the currents, i_f and i_{rf}, are partially the result of the concentrated nature of the shorted turns in space, thus no harmonic filtering due to winding factor effects is present. Also, the fact that in the strictly two-dimensional TSFE and MEC models end-leakage inductance effects are not included, while in the actual test results such end-leakage inductance effects are inherently embedded in the physical nature of the equipment, leads to the noticeable harmonic overestimation in the fault currents of Figs. 7a and 7b when compared to the experimental results of Fig. 7c.

In addition, shown in Figs. 8 and 9 is the dependence of the current passing through the fault resistance, i_{rf}, on the value of fault resistance, r_f, for both the MEC and TSFE models, and the experimental tests for, $N_{st}=2$, and, $N_{st}=6$, shorted turns. Here, it should be noted that in the experimental tests the fault current has been limited to $\sim 20A_{rms}$ in order to avoid permanent damage to the stator winding. From Figs. 7, 8 and 9 one should note that at the initial stages of a fault, the fault current is inversely proportional to the fault resistance.

C. *Rotor Faults* (*Broken/Cracked Bars*)

Here, simulation and experimental results are presented for the machine operating under the conditions of broken rotor bar failure. Depicted in Figs. 10a and 10b are the frequency spectra of the phase-a currents, i_a, for the conditions of one broken bar obtained via the MEC simulation and experimental test. Shown in Fig. 11 is the dependence of the lower side band (LSB) component [9] on the number of broken rotor bars obtained from both the MEC simulations and experimental test data.

V. Conclusions

The developed magnetic equivalent circuit model shows good agreement with both experimental data and time-stepping finite-element simulations. Hence, the developed magnetic equivalent circuit model can be used in comprehensive, nondestructive studies of stator inter-turn short circuit and rotor broken bar failures in induction motors. Also, the developed MEC model can be used as a software test-bed for simulation and development of fault diagnostics and fault mitigation algorithms.

Appendix

TABLE A-I. RELEVANT MEC MODEL PARAMETERS.

Parameter	Stator	Rotor
Stator Resistance, r_s, [Ω/phase]	1.34	
Rotor bar resistance, r_b, [μΩ]		57.1
Ring resistance bar-to-bar, r_{er}, [μΩ]		3.20
Tooth reluctance, $\Re$, [H^{-1}]	$(2.71\times10^{7})/\mu_R$	$(2.69\times10^{7})/\mu_R$
Tangential permeance, P_{TAN} , [H]	4.44×10^{-7}	2.70×10^{-7} (assumed constant)
Yoke/backiron permeance, P_{YOKE} , [H]	1.27×10^{-3}	1.20×10^{-2}
Maximum value of air-gap permeance, P_{AGMAX}, [H]	4.21×10^{-6}	

μ_R = relative permeability (assume $\mu_R=11000$ in linear region)

References

[1] A. E. Fitzgerald, C. Kingsley, S. D. Umans, Electric Machinery. 6th Edition, New York, McGraw-Hill, 2003.

[2] X. Luo, Y. Liao, H. A. Toliyat, A. El-Antably, and T. A. Lipo, "Multiple Coupled Circuit Modeling of Induction Machines," *IEEE Transactions on Industry Applications*, Vol. 31, No. 2, pp. 203-210, March/April 1995.

[3] V. Ostovic, Dynamics of Saturated Electric Machines. New York, Springer-Verlag, 1989.

[4] V. Ostovic, "A Simplified Approach to Magnetic Equivalent-Circuit Modeling of Induction Machines," IEEE Transactions on Industrial Applications, Vol. 24, No. 2, pp. 308-316, March/April 1988.

[5] H. Meshgin-Kelk, J. Milimonfared, and H. A. Toliyat, "Interbar Currents and Axial Fluxes in Healthy and Faulty Induction Motors," IEEE Transactions on Industry Applications, Vol. 40, No. 1, pp. 128-134, January/February 2004.

[6] S. D. Sudhoff, B. T. Kuhn, K. A. Corzine, and B. T. Branecky, "Magnetic Equivalent Circuit Modeling of Induction Motors," IEEE Transactions on Energy Conversion, Vol. 22, No. 2, pp. 259-270, June 2007.

[7] G. Y. Sizov, "Analysis, Modeling, and Diagnostics of Adjacent and Nonadjacent Broken Rotor Bars in Squirrel-Cage Induction Machines," M.S. Thesis, Marquette University, Milwaukee, Wisconsin, USA, December 2007.

[8] J. F. Bangura, N. A. O. Demerdash, "Diagnosis and Characterization of Effects of Broken Bars and Connectors in Squirrel-Cage Induction Motors by a Time-Stepping Coupled Finite Element-State Space Modeling Approach," IEEE Transactions on Energy Conversion, Vol. 14, No. 4, pp. 1167-1176, December 1999.

[9] G. B. Kliman and R. A. Koegl, "Noninvasive Detection of Broken Rotor Bars in Operating Induction Motors," IEEE Transactions on Energy Conversion, Vol. 3, No. 4, pp. 873-879, December 1988.